THE JOURNAL OF BIOLOGICAL CHEMISTRY VOL. 288, NO. 29, pp. 20896–20907, July 19, 2013

Antimalarial Activity of Cupredoxins

*THE INTERACTION OF PLASMODIUM MEROZOITE SURFACE PROTEIN 1$_{19}$ (MSP1$_{19}$) AND RUSTICYANIN**

Received for publication, February 14, 2013, and in revised form, June 7, 2013 Published, JBC Papers in Press, June 7, 2013, DOI 10.1074/jbc.M113.460162

Isabel Cruz-Gallardo[‡1], Irene Díaz-Moreno[‡], Antonio Díaz-Quintana[‡], Antonio Donaire[§2], Adrián Velázquez-Campoy[¶3], Rachel D. Curd[‖4], Kaveri Rangachari[‖], Berry Birdsall[**], Andres Ramos[5], Anthony A. Holder[‖6], and Miguel A. De la Rosa[‡7]**

*From the [‡]Instituto de Bioquímica Vegetal y Fotosíntesis (IBVF), cicCartuja, Universidad de Sevilla-CSIC, Avenida Américo Vespucio 49, Sevilla 41092, Spain, the [§]Departamento de Química Inorgánica, Facultad de Química, Universidad de Murcia, Campus Universitario de Espinardo, Murcia 30100, Spain, the [¶]Instituto de Biocomputación y Física de Sistemas complejos (BIFI), Universidad de Zaragoza, c/Mariano Esquillor, Zaragoza 50018, Spain, the [‖]Parasitology Division and **Molecular Structure Division, Medical Research Council (MRC) National Institute for Medical Research, The Ridgeway, Mill Hill, London W7 1AA, United Kingdom*

Background: The interaction of MSP1$_{19}$ with the cupredoxin azurin inhibits the growth of *Plasmodium falciparum* in red blood cells.
Results: Rusticyanin forms a well defined complex with MSP1$_{19}$ upon binding at the same surface area than inhibitory antibodies.
Conclusion: Rusticyanin becomes an excellent therapeutic agent for malaria.
Significance: Knowing the rusticyanin-MSP1$_{19}$ interface will allow the design of novel antimalarial drugs.

The discovery of effective new antimalarial agents is urgently needed. One of the most frequently studied molecules anchored to the parasite surface is the merozoite surface protein-1 (MSP1). At red blood cell invasion MSP1 is proteolytically processed, and the 19-kDa C-terminal fragment (MSP1$_{19}$) remains on the surface and is taken into the red blood cell, where it is transferred to the food vacuole and persists until the end of the intracellular cycle. Because a number of specific antibodies inhibit erythrocyte invasion and parasite growth, MSP1$_{19}$ is therefore a promising target against malaria. Given the structural homology of cupredoxins with the Fab domain of monoclonal antibodies, an approach combining NMR and isothermal titration calorimetry (ITC) measurements with docking calculations based on BiGGER is employed on MSP1$_{19}$-cupredoxin complexes. Among the cupredoxins tested, rusticyanin forms a well defined complex with MSP1$_{19}$ at a site that overlaps with the surface recognized by the inhibitory antibodies. The addition of holo-rusticyanin to infected cells results in parasitemia inhibition, but negligible effects on parasite growth can be observed for apo-rusticyanin and other proteins of the cupredoxin family. These findings point to rusticyanin as an excellent therapeutic tool for malaria treatment and provide valuable information for drug design.

Malaria is a widely spread disease causing morbidity and mortality throughout a large part of the world. The increasing resistance of *Plasmodium falciparum*, the causative agent of the most deadly form of the disease, to current drugs has only increased the urgency for finding new antimalarial agents (1, 2), including an effective vaccine and new drug therapies (3, 4). There are five *Plasmodium* species that infect humans, whereas others infect other primates or rodents. Among this latter group, rodent parasites such as *Plasmodium yoelii* provide useful laboratory models for the study of malaria. The disease is caused by the replication and multiplication of the asexual blood stages in red blood cells. The merozoite form of the parasite invades the host cell, where it develops and replicates to form several new merozoites that then burst out of the cell to continue the cycle of invasion and multiplication. The invasion of red blood cells requires an initial recognition and binding mediated by parasite surface ligands, followed by reorientation and the formation of a moving junction between the erythrocyte and merozoite surfaces as the parasite enters the cell. Merozoite surface protein-1 (MSP1)[8] has been implicated in this initial binding between parasite and host cell.

Located on the surface of the asexual blood-stage schizont and merozoite, MSP1 is one of the most frequently studied molecules of the parasite (5). It is synthesized as a ~200-kDa

* This work was supported in part by Junta de Andalucía Grants P08-CVI-3876 and BIO198 (Spain) and European Social Fund-ERDF 2007–2013.
[1] Supported by Junta de Andalucía Ph.D. Grant P08-CVI-3876 and GERMN bursaries for short term stays (Spain).
[2] Supported by Ministerio de Economía y Competitividad Grant SAF2011-26611 and Fundación Séneca de la Región de Murcia Grant 15354/PI/10 (Spain).
[3] Supported by Ministerio de Ciencia e Innovación Grant BFU2010-19451 (Spain).
[4] Recipient of a Medical Research Council studentship.
[5] Supported by Medical Research Council Grant U117574558.
[6] Laboratory work supported by Medical Research Council Grant U117532067 and the European Union FP7 Network of Excellence EviMalar.
[7] To whom correspondence should be addressed. Tel.: 34-954489506; Fax: 34-954460065; E-mail: marosa@us.es.

[8] The abbreviations used are: MSP1, merozoite surface protein-1; Az, azurin; BiGGER, bimolecular complex generation with global evaluation and ranking; HSQC, heteronuclear single-quantum coherence; ITC, isothermal titration calorimetry; mAb, monoclonal antibody; MSP1$_{19}$, MSP1 19-kDa C-terminal fragment; Pc, plastocyanin; PDB, Protein Data Bank; Rc, rusticyanin.

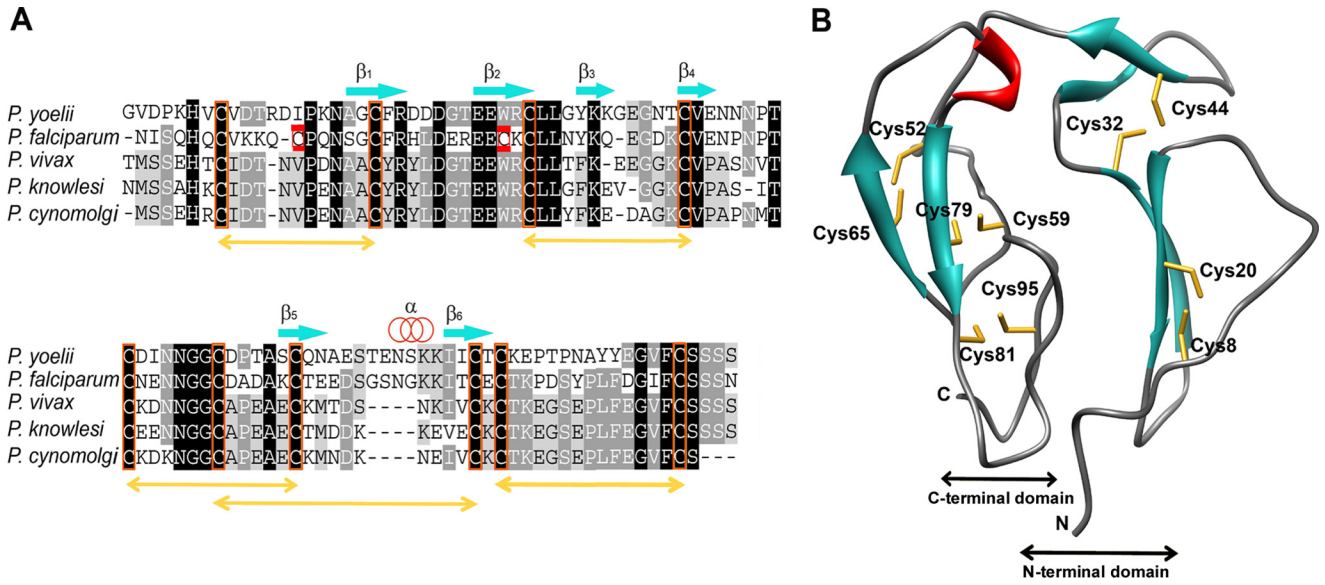

FIGURE 1. **MSP1$_{19}$ protein.** *A*, multiple sequence alignment of MSP1$_{19}$ with ClustalW2 (18) from a number of *Plasmodium* species. Sequences are colored by percent identity: *black* (100%), *dark gray* (80%), *light gray* (60%), and *white* (<50%). Secondary structure elements of *P. yoelii* MSP1$_{19}$ are shown. *Orange boxes* highlight cysteine residues that are conserved across different *Plasmodium* species, whereas *red boxes* highlight those present only in *P. falciparum*. *Gold arrows* stand for disulfide bonds formed by cysteine residues. The main difference between *P. falciparum* MSP1$_{19}$ and homologs from other *Plasmodium* species characterized to date lies in the disulfide bond pattern of the protein from the other species: one of the cysteine pairs in the first EGF domain is substituted by a tryptophan and a nonpolar or aliphatic residue. *B*, ribbon representation of the lowest energy NMR structure of *P. yoelii* MSP1$_{19}$ (BMRB accession number: 19233). Side chains of cysteine residues forming disulfide bridges are represented in *gold*.

precursor attached to the surface of the parasite via a glycosylphosphatidylinositol anchor, which undergoes a two-step proteolytic process: first, at merozoite release and then at erythrocyte invasion (6). As a result of this processing, the MSP1 is cleaved into several polypeptides that are shed from the surface in the final processing step, save a 19-kDa C-terminal fragment (MSP1$_{19}$). MSP1$_{19}$ is retained on the parasite surface by the glycosylphosphatidylinositol anchor and taken into the red blood cell at invasion (7–9). The role of MSP1$_{19}$ in the subsequent intracellular development of the parasite is poorly understood, although it is transferred to the developing food vacuole, where it remains until the end of the intracellular cycle and is discarded in the residual body together with products of hemoglobin digestion such as hemozoin (10). MSP1$_{19}$ is considered a promising malaria vaccine candidate due to the abundant evidence of specific antibodies inhibiting erythrocyte invasion and parasite growth, for instance, via the disruption of MSP1 proteolytic processing and intracellular parasite development (11).

At the structural and functional levels, MSP1$_{19}$ is particularly well conserved among *Plasmodium* species (Fig. 1) (12–17), and its three-dimensional structure has been shown to consist of two epidermal growth factor (EGF)-like domains in close contact. A characteristic disulfide-bridge pattern (Fig. 1) makes MSP1$_{19}$ highly resistant to proteases (19) and may explain why MSP1$_{19}$ remains intact in the digestive food vacuole up to the end of the intracellular cycle (10).

MSP1-specific immunoglobulins react with conformational epitopes of MSP1$_{19}$. Some of these antibodies inhibit parasite invasion of erythrocytes, whereas others do not. Fine structure epitope mapping of different monoclonal antibodies (mAbs) and the use of NMR methods indicates the binding of two inhibitory antibodies to epitopes on one side of the molecule near the interface between the two EGF domains, including residues from both domains (20, 21). By contrast, non-inhibitory neutral mAbs bind elsewhere on the molecule (15, 20). Here, we have used MSP1$_{19}$ from *P. yoelii*, a rodent malaria parasite used as a laboratory model for vaccine studies (22) and for which both inhibitory and neutral antibodies have been partially mapped on the structure (23, 24).[9] Independently of the immunoglobulin class, complexes involving MSP1$_{19}$ are kinetically rather stable with dissociation constants in the micromolar to subnanomolar range (15, 25).[10] Because the binding affinity is similar in all cases, it has been assumed that the inhibitory effect depends mainly on steric factors, namely, epitope location, rather than the nature of the antibody.

The present study has been based on the structural homology of cupredoxins with the Fab fragment of an antibody, as well as on reports of a protein from this family interacting directly with MSP1$_{19}$ and blocking the increase of parasitemia in human red blood cells infected by *P. falciparum*, suggesting a promising treatment (26, 27). We first used the DaliLite pairwise comparison program to identify structural similarities between cupredoxins and the Fab fragment (28). A screening was then performed combining NMR and ITC measurements with docking calculations using BiGGER which indicated that, among the cupredoxins tested, rusticyanin (Rc) provided the most effective binding to MSP1$_{19}$. The two proteins form a well defined complex where Rc interacts at the interface between the two MSP1$_{19}$ subdomains, at a site that overlaps with the surface recognized by the inhibitory antibodies. Further, *P. falciparum* growth is inhibited by the presence of Rc in red blood cell cul-

[9] R. D. Curd and A. A. Holder, unpublished data.
[10] M. J. Lock and A. A. Holder, unpublished data.

tures. Interestingly, the copper site plays a key role in complex formation, because apo-Rc is not only unable to interact with $MSP1_{19}$, but also to inhibit parasite invasion and development in infected red blood cells.

EXPERIMENTAL PROCEDURES

Expression and Purification of Proteins—P. yoelii $MSP1_{19}$ (^{15}N-labeled or unlabeled) was produced (essentially as described previously (29)) from a synthetic gene optimized for *Pichia pastoris* expression using as nitrogen source either $^{15}NH_4Cl$ or $(NH_4)_2SO_4$ for labeled and unlabeled protein, respectively. The 99-amino acid sequence corresponds to residues 1656–1754 of the UniProtKB entry P13828 containing the N-terminal tag HHHHHHIEGR that has little effect on the NMR spectrum (20). Secreted His_6-tagged $MSP1_{19}$ was purified from the culture medium by nickel affinity chromatography (Ni-Sepharose 6 Fast Flow; GE Healthcare) and according to a previously elaborated protocol (12).

All recombinant metalloproteins were expresed in *Escherichia coli* cultures in LB medium and purified according to previously elaborated procedures, namely *Acidithiobacillus ferrooxidans* Rc (30, 31), *Nostoc* sp. PCC 7119, *Phormidium laminosum* and poplar plastocyanins (Pc) (32–34) and *Pseudomonas aeruginosa* azurin (Az) (35).

NMR Spectroscopy—All protein samples were concentrated in 10 mM potassium phosphate (pH 6.5) using Millipore 3000 NMWL centricons and microcons. $MSP1_{19}$ samples ranged in concentration from 0.5 to 2 mM, whereas cupredoxins were used in the range of 2–5 mM. All NMR samples contained 10% D_2O to adjust the lock signal. Reduction of the metal center in samples of copper(I) cupredoxins was achieved by adding sodium ascorbate, whereas oxidation of the metal center in samples of copper(II) proteins was achieved using sodium ferricyanide for Pc and Az, and sodium hexachloroiridate(IV) for Rc. In all cases, the proteins were washed extensively to remove the excess of the reducing/oxidizing agent.

NMR experiments were performed in a Bruker Avance 600 MHz spectrometer at 25 °C. The sequence-specific assignment of the backbone amide groups of ^{15}N $MSP1_{19}$ (BMRB accession number: 19233) was achieved using standard backbone experiments (HNCACB, HNCA, etc.) and was confirmed using three-dimensional ^1H-^{15}N NOESY-HSQC and three-dimensional ^1H-^{15}N total correlation spectroscopy-HSQC spectra. The interaction of $MSP1_{19}$ with cupredoxins was followed by acquiring two-dimensional ^1H-^{15}N HSQC spectra during the titration of 0.5 mM ^{15}N-$MSP1_{19}$ solutions with an increasing amount of oxidized or reduced cupredoxins up to a final cupredoxin:$MSP1_{19}$ molar ratio of 4:1. The pH value of the sample was verified after each titration step. Prolines, which are invisible resonances in ^{15}N HSQC spectra, are located at the positions 4, 15, 50, 61, 84, and 86, whereas Gly-1, Val-2, Glu-69, and Asn-73 are unassigned residues. All data processing was performed with Bruker TopSpin 2.0, and NMR analysis of line broadening perturbations of the cupredoxin-bound $MSP1_{19}$ with respect to free malarial protein was performed in the SPARKY program (36).

NMR Line Width Analysis—To estimate line widths, the peaks were fitted to a Gaussian function for the ^{15}N and ^1H dimensions using the program SPARKY with a 10,000 steps minimization and a 0.05% tolerance. In the analysis of the line widths ($\Delta\nu_{1/2}$), the overall broadening ($\Delta\Delta\nu_{1/2}$) obtained from signals displaying only minor line broadening was first subtracted from the line width of the corresponding signal. Then, for each residue, the differences of line widths between free and interacting $MSP1_{19}$ were calculated in every titration series ($\Delta\Delta\nu_{1/2\ \mathrm{Binding}}$). The threshold value, used to identify a specifically broadened residue when data from the titration series were analyzed together, was defined as the average $\Delta\Delta\nu_{1/2\ \mathrm{Binding}}$ for the system plus 2 standard deviations ($2S_{n-1}$). The average $\Delta\Delta\nu_{1/2\ \mathrm{Binding}}$ and standard deviation were calculated for all amides with values $\leq$10 Hz on the basis that data $>$10 Hz clearly indicated a specifically broadened residue, and their inclusion would bias the average to a higher value. Some assigned signals of the free $MSP1_{19}$ HSQC spectrum overlap (Val-9, Asn-87, and Cys-95) or exhibit very low intensity (Gly-41 and Asn-42), so they could not be properly integrated to include them in the line width analysis.

ITC—All ITC experiments were performed using VP-ITC and Auto-ITC200 instruments (Microcal; GE Healthcare) at 25 °C titrating Rc with $MSP1_{19}$. The reference cell was filled with distilled water. The experiments consisted of 10-μl or 2-μl injections of 0.3 mM $MSP1_{19}$ solution in 10 mM potassium phosphate buffer (pH 6.5) into the sample cell, initially containing 6.67 μM Rc solution (reduced, oxidized, and apo forms) in the same buffer. All of the solutions were degassed before the titrations were performed. Titrant was injected at appropriate time intervals to ensure the thermal power signal returned to the base line prior to the next injection. To achieve homogeneous mixing in the cell, the stirring speed was kept constant at 1000 rpm in the Auto-ITC200 and at 450 rpm in the VP-ITC. The data, specifically the heat per injection normalized per mol of injectant *versus* molar ratio, were analyzed with Origin 7 (Microcal) using a single-site binding model. Calibration and performance tests of the calorimeter were carried out conducting $CaCl_2$-EDTA titrations with solutions provided by the manufacturer.

Molecular Docking Simulations—A soft docking algorithm implemented in the BiGGER software package (37) was used to determine *in silico* a model of the complexes $MSP1_{19}$-Az, $MSP1_{19}$-Pc, and $MSP1_{19}$-Rc. The PDB coordinates files of cupredoxins were 1JZG for Az (38), 1NIN for Pc (39), and 1A3Z for Rc (40). For each run, 5000 docking geometric solutions were generated based on the complementarity of the protein surfaces. These solutions were evaluated and ranked according to their "global score" and different interaction criteria including electrostatic energy of interaction, relative solvation energy, and the relative propensity of side chains to interact. For the $MSP1_{19}$-Rc adduct, NMR restraints were introduced in the docking calculations. All complexes graphic images were generated using the UCSF Chimera package (41).

P. falciparum Cultures—Synchronized *P. falciparum* 3D7 late stage trophozoites at 33–36 h were used. The final parasitemia and hematocrit were between 0.1–0.2 and 2%, respectively. Red blood cells used for the assay were centrifuged to remove the buffy coat and washed twice in RPMI 1640 medium so that no white blood cells were present. The cul-

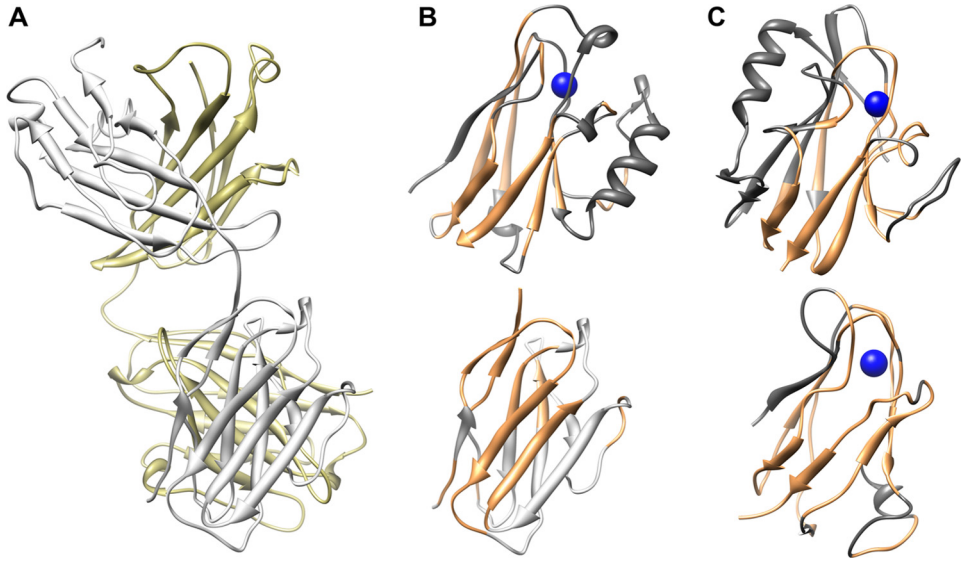

FIGURE 2. **Conserved structural motifs.** *A*, ribbon representation of the Fab fragment of mAb G17.12 (PDB ID code 1OB1). Domain A is depicted in *light gray* and domain B in *gold*. *B*, structural alignment of Az (*upper*, PDB ID code 1JZG) and A1 fragment of Fab (*lower*) built by DaliLite pairwise comparison server. Matching regions, with a Dali *Z*-score of 2.9, appear in *orange*. *C*, ribbon representation of Rc (*upper*, PDB ID code 1A3Z) and Pc (*lower*, PDB ID code 1NIN). Dali *Z*-scores for Rc and Pc are 2.6 and 3.1, respectively. Copper atoms are colored in *blue*.

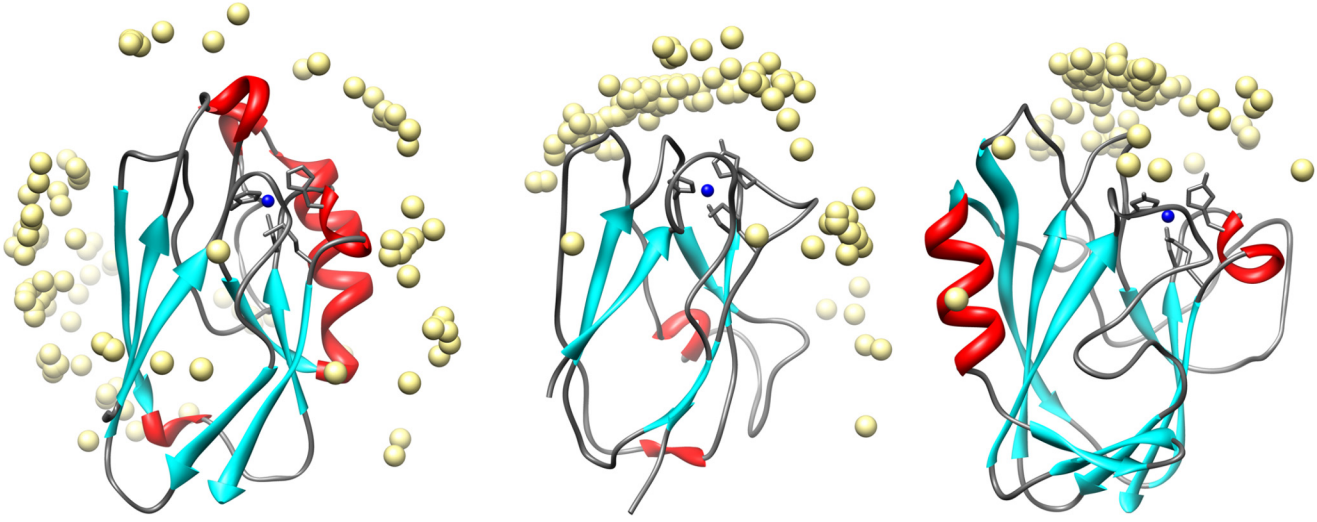

FIGURE 3. ***Ab initio* docking of cupredoxins with MSP1$_{19}$ performed by BiGGER.** *Left*, Az. *Center*, Pc. *Right*, Rc. *Light yellow spheres* represent the geometry centers of MSP1$_{19}$ in the 100 best solutions generated for each complex. All cupredoxins are oriented with respect to their copper center. Robertson diagrams of the cupredoxins are colored according to secondary structures: α-helices in *red* and β-strands in *blue*. Copper atoms are represented as *blue spheres* and the residues bonding to them are in *gray sticks*.

ture medium contained RPMI 1640 medium supplemented with 5 g/liter albumax, 0.025 g/liter gentamycin, and 0.292 g/liter L-glutamine.

P. falciparum Growth Inhibition Assay—Sterile 96-well black tissue culture plates (Costar) were used routinely for every assay. The holo- or apo-species of Rc and *Nostoc* Pc were diluted in culture medium and used in duplicate wells for each dilution (200, 100, 50, and 25 μM, respectively) in a final volume of 100 μl/well. Two control sets were used in duplicate wells, one set with no added cupredoxin (positive control) and one with uninfected red blood cells (negative control). The plates were incubated at 37 °C for 48 h in a gas chamber flushed with 5% CO_2, 5% O_2, and 90% N_2. After 48 h, supernatants were removed from each well, replaced with fresh medium containing protein, and incubated for a further 48 h in the same manner. At the end of the 96-h incubation, 25 μl of SYBR Green I dye (SYBR Green I nucleic acid gel stain 10,000×, in dimethyl sulfoxide from Invitrogen) in lysis buffer (1 μl dye to 1 ml lysis buffer), was added to each well and stored overnight at −20 °C. The lysis buffer contained Tris-HCl (20 mM, pH 8.0), EDTA (2 mM), Saponin (0.16% w/v) and Triton X-100 (1.6% v/v). Plates were thawed at room temperature, and fluorescence intensity was measured with a FLUO Star Omega microplate fluorescence reader (BMG Labtech). Values were expressed in relative fluorescence units. Binding of SYBR Green is specific for parasite DNA as mature erythrocytes lack DNA and RNA. Fluorescence intensity unit was converted to percentage (%) of growth as follows: % growth = (culture under Rc or Pc) − (uninfected RBC)/(culture with no Rc or Pc) − (uninfected RBC) ×100, where RBC are red blood cells.

RESULTS

Structural Similarities between Cupredoxins and the Fab Fragment of a mAb—The Fab fragment crystal structure of mAb G17.12 (15), shown to bind MSP1$_{19}$, is composed of two domains, A and B, containing two regions, variable (symbolized by 1) and constant (symbolized by 2), with the canonical β-sandwich fold of the immunoglobulin superfamily (Fig. 2*A*). Consistent with previous reports, the DaliLite pairwise comparison program (28) identified significant structural similarities between the A1 fragment of the mAb and copper-containing redox proteins with immunoglobulin fold, such as Az, Pc, and Rc. In particular, the structural alignment between the A1 fragment and Az reveals a matching region, which is localized mainly at the two antiparallel β-sheets, as described previously (26; Fig. 2*B*), and with a Dali *Z*-score of 2.9. For the two other cupredoxins, Pc and Rc, this structural match is extended to the loops connecting β-strands yielding *Z*-scores of 3.1 and 2.6, respectively (Fig. 2*C*).

Given the structural similarity between various cupredoxins and the Fab fragment, *ab initio* docking approaches were performed with no experimental restraints (Fig. 3) to explore the capability of the metalloproteins to interact with MSP1$_{19}$ from *P. yoelii*. MSP1$_{19}$ is well conserved among the species with >50% sequence identity (Fig. 1*A*), with conserved three-dimensional structure and common functional features (17). We used the BiGGER rigid docking algorithm to generate sets of possible orientations for the different cupredoxin probes around MSP1$_{19}$ (the target). Fig. 3 shows the distribution of MSP1$_{19}$ mass centers resulting from the 100 best solutions from each computation around the corresponding copper protein. For Az and Pc, we observe a remarkably broad dispersion of the MSP1$_{19}$ geometry centers, suggesting the lack of specific surface complementarity. By contrast, molecular docking for the Rc-MSP1$_{19}$ interaction indicates that MSP1$_{19}$ explores a well defined area of Rc surrounding its copper center.

MSP1$_{19}$ Interactions with Cupredoxins by NMR—The MSP1$_{19}$-cupredoxin interaction was monitored by recording two-dimensional ^{15}N HSQC NMR spectra on ^{15}N-MSP1$_{19}$, both free and following the addition of Az, Pc, or Rc. The absence of changes in MSP1$_{19}$ resonances, either chemical shift perturbations or line broadening, indicates no detectable binding to Az and Pc in any of their oxidation states (Fig. 4, *top* and *middle* panels). By contrast, line width changes of certain MSP1$_{19}$ amide signals upon addition of Rc(Cu^{+}) suggest a specific MSP1$_{19}$-Rc interaction (Fig. 4, *bottom panel*). Such observations coincide with *ab initio* docking simulations performed (Fig. 3) which suggested a well defined complex only between Rc and MSP1$_{19}$.

To probe in greater detail the interaction of MSP1$_{19}$ with either oxidized or reduced Rc, we analyzed the line widths of MSP1$_{19}$ resonances from ^{15}N HSQC spectra across several titrations. Binding to Rc results in general signal broadening due to the increase in the rotational correlation time of MSP1$_{19}$ when interacting with Rc. In addition, several MSP1$_{19}$ backbone amides clustered in one area of the structure undergo larger changes in line widths ($\Delta\Delta\nu_{1/2\ \mathrm{Binding}}$) upon Rc binding (Figs. 5 and 6). These resonances are expected to be at or in the proximity of the area of MSP1$_{19}$ interacting with Rc. To selectively define resonances most likely to be part of the interface, threshold values (specifically, $\Delta\Delta\nu_{1/2\ \mathrm{Binding}} \geq 5$Hz for ^{15}N and ≥ 11Hz for ^{1}H dimension) were set (see "Experimental Procedures"). As expected, the distribution of line width changes ($\Delta\nu_{1/2}$) becomes broader as the Rc:MSP1$_{19}$ ratio increases (data not shown).

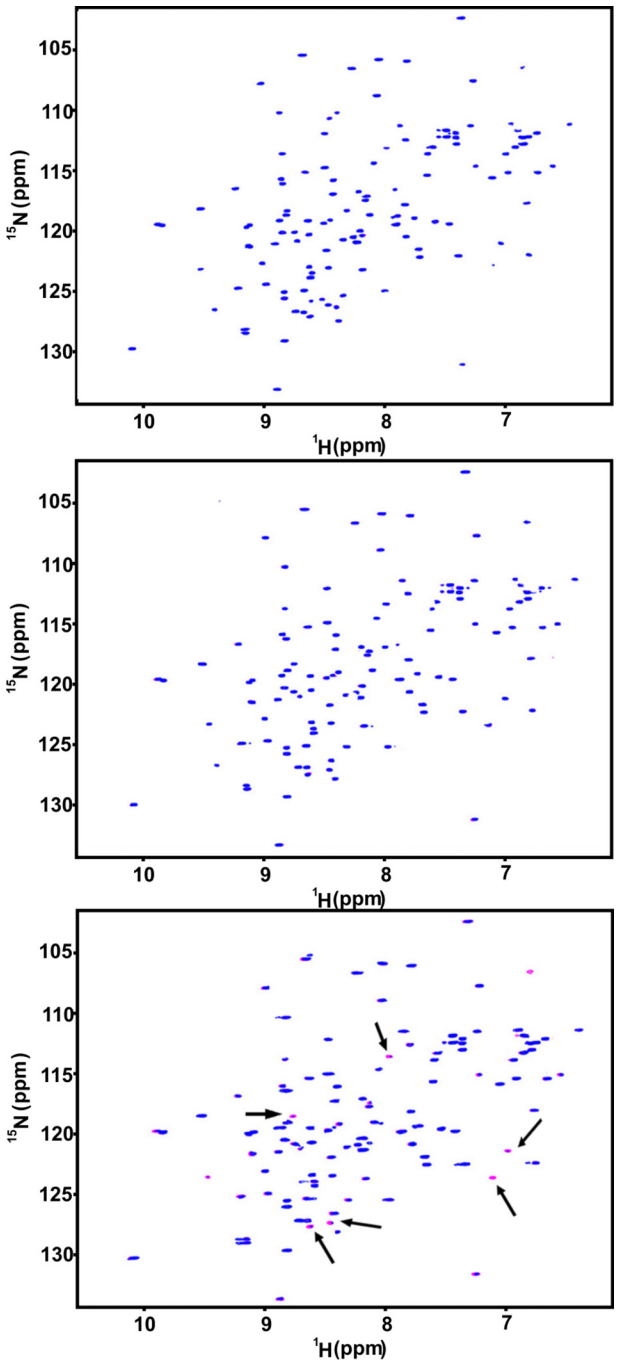

FIGURE 4. **NMR titrations of ^{15}N MSP1$_{19}$ with reduced cupredoxins.** *Top*, Az from *P. aeruginosa*. *Middle*, Pc from *Nostoc* sp. PCC 7119. *Bottom*, Rc from *A. ferrooxidans*. Superimposition of ^{15}N HSQC spectra of free MSP1$_{19}$ (*magenta*) and after adding one of three cupredoxins (*blue*) at a cupredoxin:MSP1$_{19}$ ratio of 4:1 is shown. *Arrows* point out those residues that experience substantial broadening. Negligible binding to MSP1$_{19}$ was observed upon adding aliquots of Pc and Az.

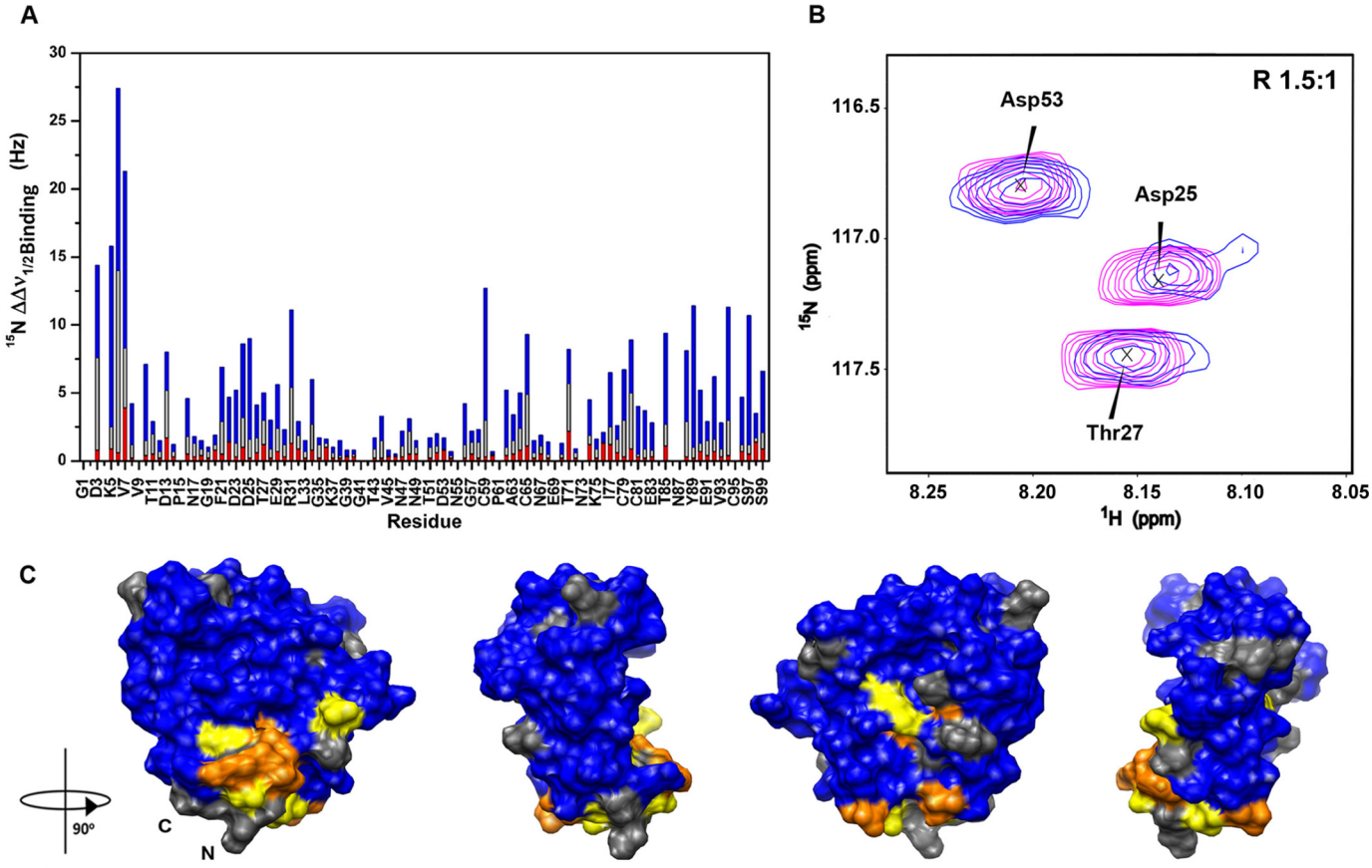

FIGURE 5. **NMR titration of ^{15}N MSP1$_{19}$ with reduced Rc.** *A*, ^{15}N line width differences (^{15}N $\Delta\Delta\nu_{1/2\ Binding}$) between free and Rc-bound MSP1$_{19}$. The Rc:MSP1$_{19}$ ratios are 0.5:1 (*red*), 1:1 (*gray*), and 1.5:1 (*blue*). *B*, superposition of ^{15}N HSQC spectra of free MSP1$_{19}$ (*magenta*) and bound to Rc (*blue*) in a Rc:MSP1$_{19}$ ratio of 1.5:1. A subset of three representative resonances is labeled in *black*. *C*, map of MSP1$_{19}$ interface upon binding to Rc. MSP1$_{19}$ surface is rotated 90° around the vertical axes in each view. Residues are colored according to their ^{15}N $\Delta\Delta\nu_{1/2\ Binding}$ (Hz): the resonances that undergo the largest broadening (≥5 Hz) are *orange*, and the signals with a significant line width over the detection limit <5 Hz are *yellow*. The limit of 5 Hz corresponds to a threshold value relative to the average plus 2-fold the S.D. ($\Delta\Delta\nu_{1/2\ Binding} \geq <\Delta\Delta\nu_{1/2\ Binding}> + 2S_{n-1}$). Residues with no line width perturbation are marked in *blue*, whereas prolines are in *gray*.

At the Rc(Cu^{1+}):MSP1$_{19}$ ratio of 1.5:1, 14 amino acids show considerable ^{15}N line width changes in MSP1$_{19}$ HSQC spectra (Fig. 5, *A* and *B*). These residues are distributed mainly along two regions of MSP1$_{19}$, namely, at the beginning of N-terminal EGF domain involving Asp-3, Lys-5, His-6, Val-7, Asp-10, and at the end of C-terminal domain comprising Thr-85, Ala-88, Tyr-89, Phe-94, and Ser-97. In addition, Asp-24, Asp-25, and Arg-31 at the two first antiparallel β-strands, along with Cys-59, are also altered. Fig. 5*C* shows the map of MSP1$_{19}$ residues affected by Rc addition, with colors corresponding to line broadening in the ^{15}N dimension. The sequential stretches of residues detailed above form the main cluster on the MSP1$_{19}$ surface, which surrounds the two EGF domain interface. Interestingly, some of these affected residues (Asp-24, Asp-25, Arg-31 and Cys-59) are located at the rear of the protein (Fig. 5*C*). Whereas Asp-24 and Asp-25 are close to amino acids at the N terminus, Arg-31 and Cys-59 lie near Phe-94. Because these four residues are adjacent to others placed at the EGF domain interface and involved in direct contact with Rc, these line width perturbations are probably a secondary effect of binding. Similar conclusions may be inferred from ^{1}H line width analysis, although protons are more sensitive to broadening (data not shown).

NMR titration of oxidized Rc on MSP1$_{19}$ results in significant MSP1$_{19}$ line width perturbations at a Rc(Cu^{2+}):MSP1$_{19}$ ratio of 4:1, at which some signals broaden beyond the detection limit (Fig. 6*A*). The MSP1$_{19}$ resonances affected by Rc(Cu^{2+}) binding involve both N-terminal (Asp-3, Lys-5, Asp-10, and Asp-13) and C-terminal (Cys-79, Thr-85, Tyr-89, Gly-92, Phe-94, Ser-97, and Ser-98) regions, as described for the reduced system at a Rc(Cu^{1+}):MSP1$_{19}$ ratio of 1.5:1. An additional stretch (Phe-21 to Asp-24, Gly-26, Glu-29, Arg-31, and Cys-59) is also perturbed whereas His-6, Val-7, Asp-25, and Thr-27 were residues over the detection limit (Fig. 6*A*). Notably, the strength of the broadening observed for a 4:1 Rc(Cu^{2+}):MSP1$_{19}$ ratio is comparable with the one observed at a 1.5:1 Rc(Cu^{1+}):MSP1$_{19}$ ratio, indicating that MSP1$_{19}$ binds more weakly to the oxidized Rc. However, the MSP1$_{19}$ interacting surface involved in Rc recognition at a Rc:MSP1$_{19}$ ratio of 4:1 is independent of the cupredoxin redox state (Fig. 6).

Binding of MSP1$_{19}$ to Holo-Rc by ITC—ITC measurements reveal that MSP1$_{19}$ binds to Rc either in its reduced or oxidized state with a 1:1 stoichiometry at 25 °C (Fig. 7). Notably, the interaction of MSP1$_{19}$ with Rc(Cu^{1+}) is exothermic with a dissociation affinity constant (K_d) of 2 μM, whereas that with Rc(Cu^{2+}) is an endothermic process with lower binding affinity

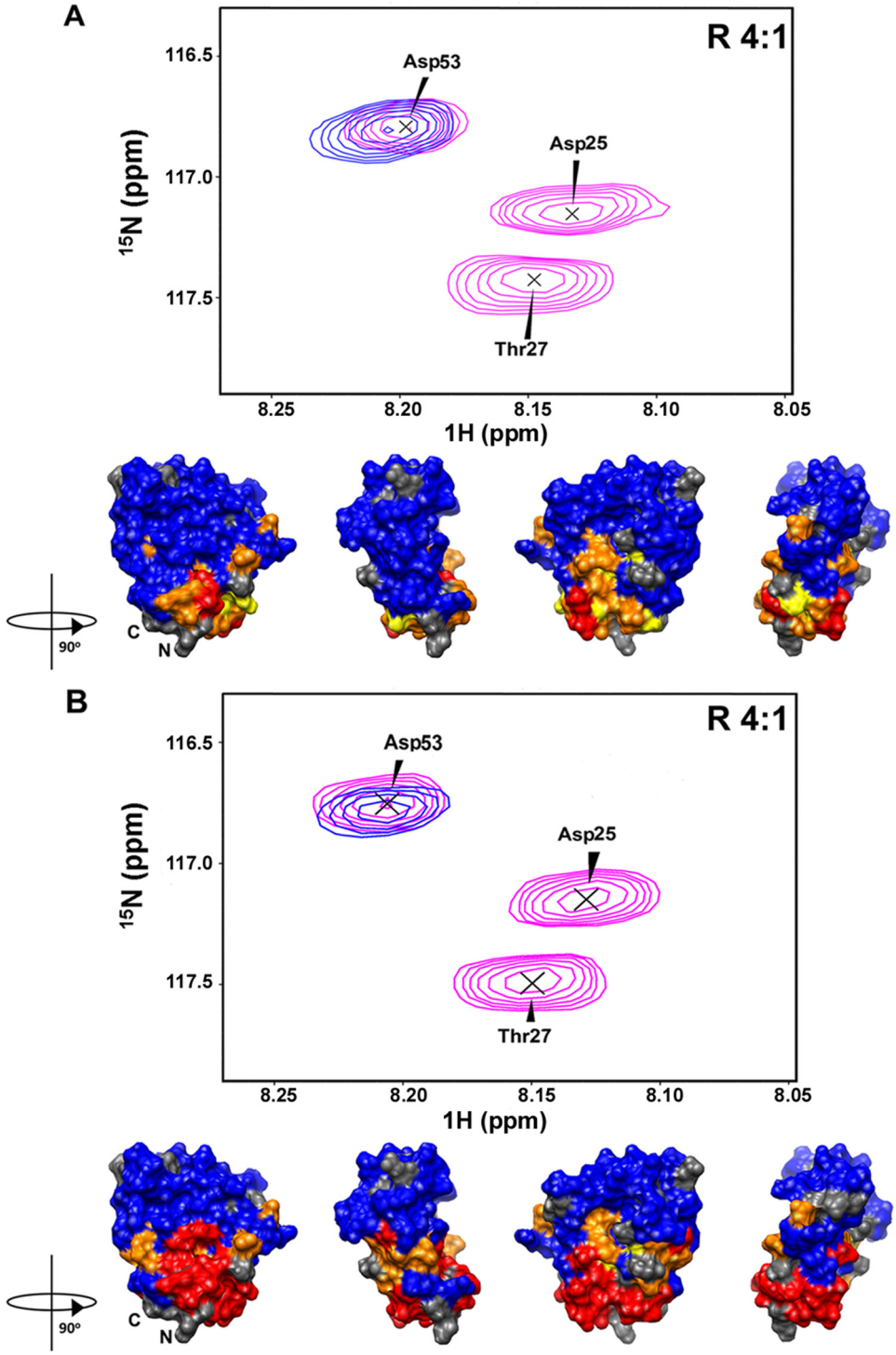

FIGURE 6. **Comparison between NMR titrations of ^{15}N MSP1$_{19}$ with either oxidized or reduced Rc at Rc:MSP1$_{19}$ ratio of 4:1.** Most of the MSP1$_{19}$ signals in binding to Rc(Cu^{1+}) are broadening over the detection limit at the Rc:MSP1$_{19}$ ratio of 4:1, suggesting that MSP1$_{19}$ binds reduced Rc with a higher affinity. *A*, *upper*, overlap between ^{15}N HSQC spectra of free MSP1$_{19}$ (*magenta*) and oxidized Rc-bound MSP1$_{19}$ (*blue*). *A*, *lower*, map of MSP1$_{19}$ in the presence of oxidized Rc. *B*, the same as *A* with reduced Rc. The 90°-rotated surface representations of MSP1$_{19}$ show residues colored according their ^{15}N $\Delta\Delta\nu_{1/2\ \mathrm{Binding}}$ following the same color code as in Fig. 5*C*. Those residues broadened beyond the detection limit are highlighted in *red*.

(K_d = 25 μM) (Table 1). Such differences in K_d values are in agreement with NMR titrations and suggest that MSP1$_{19}$ binds to reduced Rc with a greater affinity than to oxidized Rc. Further experiments need to be performed to explain the opposite sign in the enthalpy of both processes as it could be related to (i) changes in the protonation/deprotonation equilibrium of ionizable groups of the interacting proteins; (ii) variations in the hydrogen-bonding networks; (iii) differences in water arrangement in the vicinity of oxidized or reduced cofactors; and (iv) slight conformational modifications altering the number of solvent molecules excluded from the protein interface.

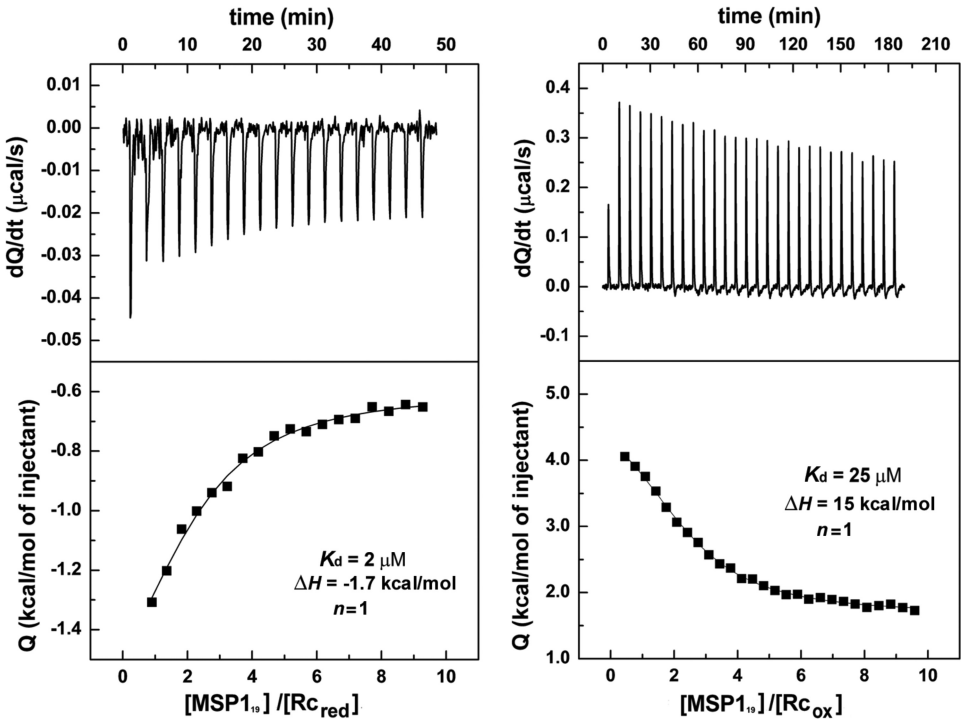

FIGURE 7. **ITC titrations of MSP1$_{19}$ with both redox states of Rc.** Binding assays of the complexes between MSP1$_{19}$ and reduced (*left*) or oxidized Rc (*right*) are shown. Thermograms are shown at the *top* and binding isotherms at the *bottom*, along with the dissociation constant (K_d expressed in μM), enthalpy (ΔH in kcal/mol). The stoichiometry value (*n*) was fixed to avoid degeneracy in the nonlinear regression data analysis. Typical relative errors are 20–25% for the dissociation constant and 5–10% for the stoichiometry.

TABLE 1

Thermodynamic values inferred from ITC experiments

The affinity of a protein-protein interaction is defined by the Gibbs energy of the binding: $\Delta G = -RT \ln K_a$. ΔG has two different contributions, ΔH and ΔS, according to the equation: $\Delta G = \Delta H - T\Delta S$, thus several combinations of those values could yield similar binding affinities. The complex formation is entropically driven in both cases, being the enthalpic contribution to the binding unfavorable (15 kcal/mol with oxidized Rc) or only slightly favorable (−1.7 kcal/mol with reduced Rc).

MSP1$_{19}$ complex	ΔG	ΔH	$-T\Delta S$	K_d
	kcal/mol	*kcal/mol*	*kcal/mol*	μM
Oxidized Rc	−6.3	15.0	−21.3	25.0
Reduced Rc	−7.8	−1.7	−6.1	2.0

The Case of Apo-Rc—To determine the role of the copper center, NMR and ITC titrations were carried out using MSP1$_{19}$ and apo-Rc. Surprisingly, NMR titrations showed no substantial line width changes even at an apo-Rc:MSP1$_{19}$ ratio of 4:1 (Fig. 8). The finding was further corroborated by ITC measurements, as the weak calorimetric profile suggests a lack of interaction (Fig. 8). Altogether, these data indicate the relevance of the copper center in the binding to MSP1$_{19}$. Despite the small structural differences in cupredoxins reported previously in solid state, there exists a high degree of mobility of the metal-binding loops in solution in the apo form, as recently demonstrated by NMR (42, 43). The different pattern between apo- and holo-Rc *versus* MSP1$_{19}$ could be related with the found differences in the dynamics of this site in the two forms.

Docking Simulations with BiGGER—Along with the *ab initio* docking calculations run on the MSP1$_{19}$-Rc(Cu$^+$) complex, revealing how the MSP1$_{19}$ mass center docks on the Rc metal crevice (Fig. 3), an NMR-restrained docking with BiGGER was also performed. Line width data for those MSP1$_{19}$ residues in contact with Rc at a Rc:MSP1$_{19}$ ratio of 1.5:1 were included in the run. The output is a set of docked solutions that can be ranked according to the BiGGER global score or individual scores, such as hydrophobic criteria, electrostatics, and geometrical parameters. Fig. 9 shows the best 100 solutions, as represented by Rc geometry centers, according to the global and hydrophobic scores from the program (Fig. 9*A*). The best scoring models predicted by restrained docking reveal how MSP1$_{19}$ leans its EGF domain interface to approach Rc (Fig. 9*A*). Indeed, the proximity of the surfaces on both proteins in the complex is shown in the space-filling representation (Fig. 9*A*). In addition to the copper center, loops connecting Rc β-strands are in close contact with MSP1$_{19}$. A deep analysis of the complex interface predicted by docking points to the N-terminal and C-terminal regions of the MSP1$_{19}$ as driving complex formation as some NMR restraints are satisfied (Fig. 9*B*). In the model reported, some electrostatic interactions occur (Fig. 9*C*) because Rc residues Lys-81 and Lys-116 are close to Glu-91 and Glu-83 in MSP1$_{19}$. Furthermore, Lys-5 of MSP1$_{19}$ can interact with Glu-9 of Rc, although the Glu is partially buried. The Rc interaction surface is mainly hydrophobic with the exception of a single positive spot, Lys-81 and Lys-116, surrounded by Phe-83, Gly-82, and Trp-7 and the copper center, which, in turn, is enclosed by Met-99, Val-98, and Pro-141. This interaction mode resembles those of the copper protein Pc and cytochrome c_6 with their photosynthetic partners, cytochrome *f* and photosystem I. In such complexes, Pc and cytochrome c_6 use the hydrophobic site surrounding the copper center and the heme group (site 1) as well as their charged patch (site 2; 44, 45).

Inhibition of P. falciparum Growth by Holo-Rc—To assess the physiological relevance of the MSP1$_{19}$ binding to Rc, the growth of *P. falciparum* within red blood cells was followed in

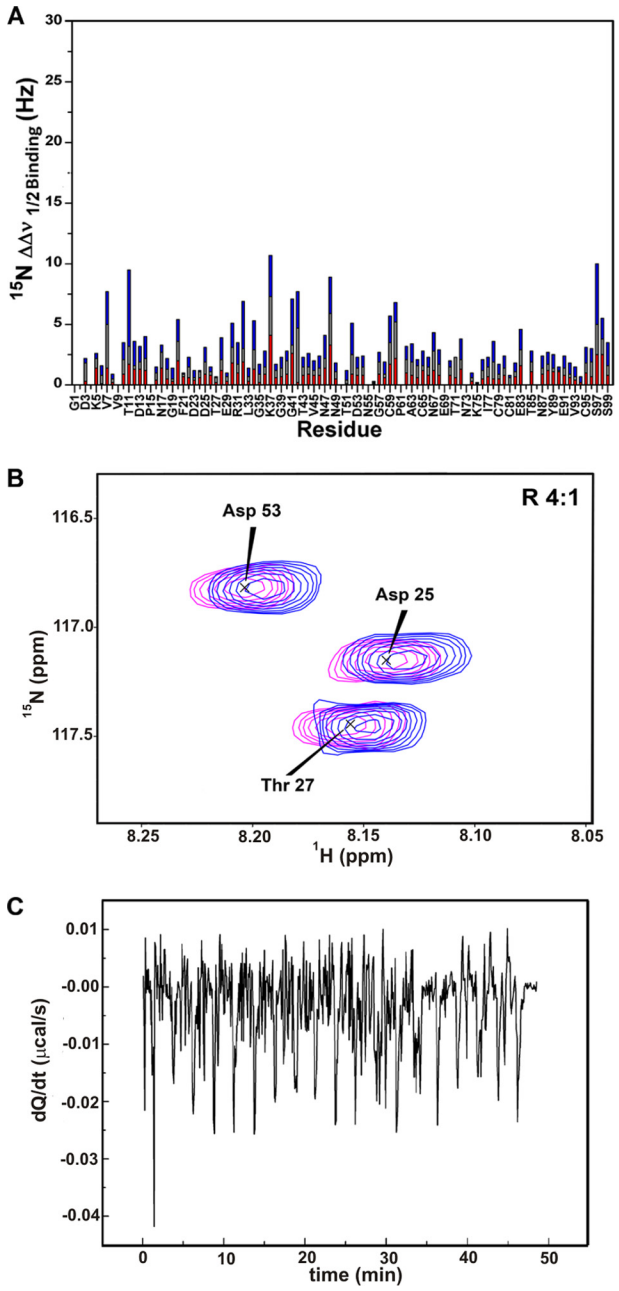

FIGURE 8. **NMR and ITC titrations of MSP1$_{19}$ with apo-Rc.** *A*, ^{15}N line width differences (^{15}N $\Delta\Delta\nu_{1/2Binding}$) between free MSP1$_{19}$ and in the presence of apo-Rc. The apo-Rc:MSP1$_{19}$ ratios were 1:1 (*red*), 1.5:1 (*gray*), and 4:1 (*blue*). *B*, overlap between ^{15}N HSQC spectra of free MSP1$_{19}$ (*magenta*) and in the presence of apo-Rc (*blue*) at an apo-Rc:MSP1$_{19}$ ratio of 4:1. *C*, ITC thermogram obtained from the apo-Rc-MSP1$_{19}$ titration, revealing the lack of binding between both proteins because of the flat calorimetric profile.

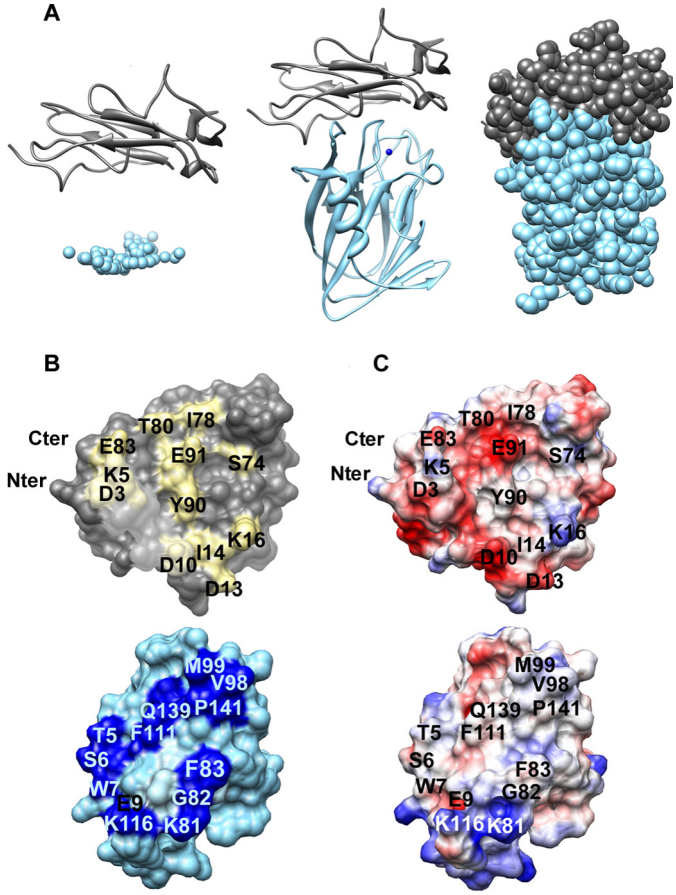

FIGURE 9. **BIGGER molecular docking of the MSP1$_{19}$-Rc complex.** *A*, *left*, best 100 models with the lowest energy values after alignment of MSP1$_{19}$ molecules with Rc geometry centers represented by *spheres*. Ribbon (*center*) and space-filling (*right*) representations for the best model are shown in the same orientation as on the *left*. MSP1$_{19}$ is represented in *dark gray* whereas Rc is in *light blue*. *B*, interface residues of the MSP1$_{19}$-Rc complex. MSP1$_{19}$ and Rc are independently rotated 90° to the top and to the bottom, respectively, with regard to their orientation in *A*. Contacting residues are depicted in *light yellow* for the MSP1$_{19}$ and *dark blue* for Rc. *C*, electrostatic potential surfaces of MSP1$_{19}$ (*upper*) and Rc (*lower*) with the same orientations as in *B*. The electrostatic potential surfaces were created with a color ramp for positive (*blue*) and negative (*red*) potentials at 300 mM ionic strength. The potentials were calculated in Chimera software (41).

the presence of either holo- or apo-Rc (see "Experimental Procedures"). The addition of holo-Rc to infected cells resulted in parasitemia inhibition, as culture growth decreased significantly (Fig. 10) at a concentration of 100 μM until the point of complete inhibition at 200 μM holo-Rc. In contrast, the apo form even at high concentrations did not have a significant effect on *P. falciparum* growth. These data fully corroborate previous observations using NMR or ITC as much as apo-Rc is unable to bind to MSP1$_{19}$.

To discard the theory that such a parasitemia inhibition could be ascribed to the well known apoptotic role of several cupredoxins (46, 47), control experiments were run with the holo- or apo-form of Pc. Holo-Pc was chosen as it does not bind to MSP1$_{19}$, as inferred from the herein presented NMR screening (see above), but it is structurally very similar to Rc: the two proteins belong to the type I blue copper-protein family, with almost identical folding and tetrahedral copper center. Upon addition of either holo- or apo-Pc (25 μM) under the same culture conditions, the *Plasmodium* growth first slightly decays to further reach a constant value until the end of the experiment. So the *Plasmodium* growth does not depend on protein concentration (the percentage of growth is maintained at approximately 70% even at 200 μM Pc) and is practically the same with either holo- or apo-Pc. Altogether these results indicate that holo-Rc inhibits parasitemia upon specific binding to MSP1$_{19}$.

DISCUSSION

Proteins from the cupredoxin family have demonstrated antimalarial activity and potential as therapeutic agents (26, 27). We have shown here that the cupredoxin rusticyanin interacts with MSP1$_{19}$ with micromolar K_d, forming a well defined complex. The interaction takes place on the same surface as that targeted by inhibitory antibodies, suggesting that a similar mechanism could take place. Its strength is dependent on the presence and, to a lesser extent, on the oxidation state of the metal center, which is consistent with the need for an intact interaction surface and charge conservation. Furthermore, we have observed the inhibition of *P. falciparum* parasitemia in infected cells where holo-Rc is present as a result of the interaction with MSP1$_{19}$. However, negligible effect on parasite growth could be observed for apo-Rc and Pc forms.

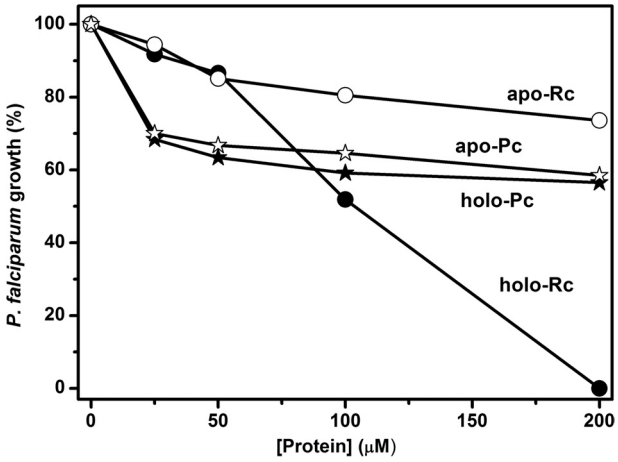

FIGURE 10. **Inhibition of *P. falciparum* growth by Rc.** Percentage of parasite growth was measured in the presence of either holo-Rc (*filled circles*), apo-Rc (*open circles*), holo-Pc (*filled stars*) or apo-Pc (*open stars*) at varying concentration (see "Experimental Procedures"). Parasite cultures were incubated with the Rc or Pc forms for a 96-h period, with a medium change after 48 h. Cultures in the absence of cupredoxin were used as a positive control.

MSP1$_{19}$ signals show slow exchange in the presence of the Fab fragments of the inhibitory mAb12.8 and mAb12.10, indicating the kinetic stability of complexes involving MSP1$_{19}$ with binding affinity constants in the micromolar to subnanomolar range (20). Rc binds specifically with a K_d of 2 μM to the interface between the two MSP1$_{19}$ EGF domains, overlapping the surface recognized by these inhibitory antibodies (20, 21), as indicated by our NMR-based mapping. A detailed comparison of MSP1$_{19}$ bound to either Rc or mAb12.10 and mAb12.8 reveals that the common interacting surfaces are located in the first EGF domain along with the first β-sheet and at the end of the second EGF domain. Interestingly, these regions of MSP1$_{19}$ form a shallow pocket (Fig. 1*B*) that may have a role in erythrocyte invasion (21). In addition, these residues involved in the formation of protein complexes with MSP1$_{19}$ are distributed in three segments: His-6 to Val-9, Lys-16 to Arg-22, and Tyr-89 to Cys-95 (numbering according to the *P. yoelii* MSP1$_{19}$ sequence; Fig. 1*A*), and they are strongly conserved in different species (21), supporting the idea that this is a functional site. The presence of additional perturbed residues identified in this study may be explained by the flat structure of MSP1$_{19}$ (5) because perturbations as a result of a protein-protein interaction may be transferred from one MSP1$_{19}$ face to the other.

Another point of interest arising from this study is the mode of interaction of MSP1$_{19}$ with Rc, compared with the interaction with mAbs. The study took as starting point a structural alignment of Rc with the Fab fragment of the non-inhibitory mAb G17.12 whose interaction with MSP1$_{19}$ has been solved through x-ray crystallography (15). The similarities with the β-barrel, as well as the loops connecting them, are clear (Fig. 2). However, the relative orientation between the mAb and MSP1$_{19}$ does not match that defined for the MSP1$_{19}$-Rc complex (Fig. 11*A*). In contrast, the models of mAb12.8-MSP1$_{19}$ and mAb12.10-MSP1$_{19}$ complexes built by Autore *et al.* (48) using NMR-based docking calculations match well with the Rc-MSP1$_{19}$ model reported here. In looking for structural sim-

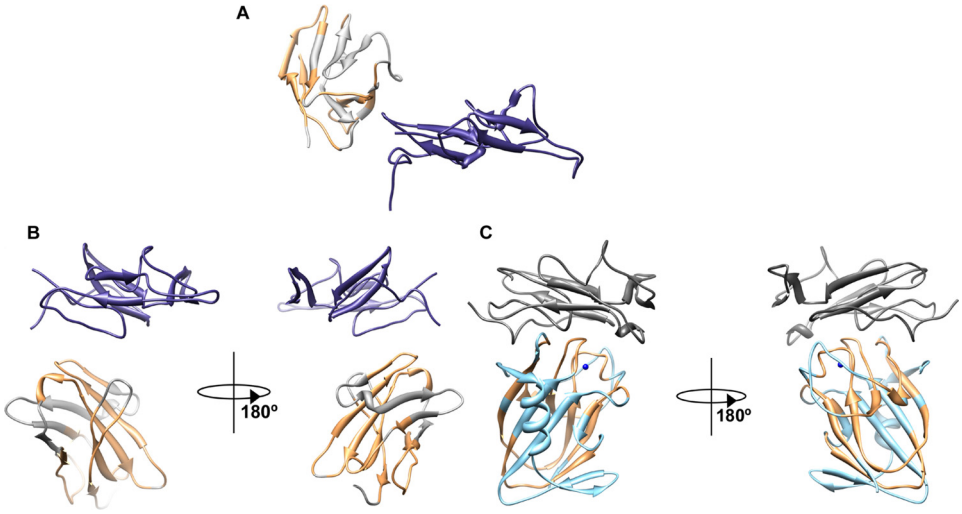

FIGURE 11. **Comparison of complexes containing MSP1$_{19}$.** *A*, MSP1$_{19}$-mAbG17.12 crystallographic structure (PDB ID code 1OB1; 15). Domain A1 of the noninhibitory mAbG17.12 is represented in *light gray*, whereas *P. falciparum* MSP1$_{19}$ is in *purple*. *B*, MSP1$_{19}$-mAb12.10 complex, whose PDB coordinates were kindly provided by Autore *et al*. (48). Domain A1 of the inhibitory mAb12.10 and *P. falciparum* MSP1$_{19}$ are colored as in *A*. *C*, MSP1$_{19}$-Rc complex studied in this work. *P. yoelii* MSP1$_{19}$ is depicted in *dark gray* and Rc in *light blue*. Copper center is represented by a *blue sphere*. Matching regions between mAbG17.12 or mAb12.10 and Rc after structural alignment using DaliLite are depicted in *orange*. The 180°-rotated views for both MSP1$_{19}$-mAb12.10 and MSP1$_{19}$-Rc complexes are shown.

ilarities between Rc and mAb12.10 with the DaliLite pairwise comparison server, the *Z*-score 2.8 (Fig. 11, *B* and *C*) suggested strong structural similarities, especially in the loops that interact with MSP1$_{19}$. In this paper, MSP1$_{19}$ complexes with mAb12.10 and Rc demonstrate (Fig. 11) a similar MSP1$_{19}$ orientation with respect to the other molecule (mAb12.10 or Rc) within each complex. The A1 region of mAb12.10 forms the main interaction with MSP1$_{19}$, similar to the structurally related region of Rc, especially at the level of β-strand connecting loops. As proposed by Autore *et al.* (48), a positively charged electrostatic spot on the antibody surface is required in the interaction and binding to MSP1$_{19}$. A similar positively charged area is located on the Rc surface, Lys-81 and Lys-116 in the complex interface, as inferred from our docking simulations (Fig. 9*C*). The Rc-MSP1$_{19}$ interface also involves hydrophobic contacts in the region surrounding the Rc copper center that presumably plays a key role in complex formation, as indicated by the NMR and ITC experiments. Reduced Rc binds MSP1$_{19}$ more efficiently than the oxidized form, suggesting that both electrostatic potential properties and protein folding depend on the metal redox state. This effect is even more drastic for apo-Rc, which is unable to interact with MSP1$_{19}$.

The practical significance of these observations can be found in the potential antimalarial role of the binding of Rc to MSP1$_{19}$ on the parasite surface, thereby blocking parasite growth and interfering directly with parasite invasion of red blood cells. In fact, the interaction might sterically interfere with the recognition between MSP1 and an erythrocyte surface molecule or with the proteolytic processing of MSP1, which occurs during invasion and can be inhibited by antibodies binding to MSP1$_{19}$. Such a role has been shown previously in the drug suramin (49). An alternative hypothesis, based on the fact that MSP1$_{19}$ is internalized with the malaria parasite during invasion and then trafficked to the food vacuole where it persists until the end of the next intraerythrocytic cycle (10), is that MSP1$_{19}$-bound Rc would be internalized and interfere with MSP1$_{19}$ functioning inside the cell, as shown for an antibody (11). Supporting this possibility, it has been reported that Rc is not only able to enter mammalian cells, but also to induce caspase-8-mediated apoptosis and/or to inhibit the cell cycle (47). Furthermore and unlike other cupredoxins, Rc is a copper protein with high acid stability and is biologically functional at a pH below 1.0 (50). The extreme acid stability of Rc may be important in understanding its function of blocking MSP1$_{19}$ because pH is ~4.5–5.5 inside the *Plasmodium* food vacuole. Altogether, Rc could be an excellent therapeutic tool for malaria treatment and expand our understanding of MSP1$_{19}$ function. In this way, as well, it could provide beneficial information for drug design.

Acknowledgments—We thank G. Kelly (London, United Kingdom) for support in recording NMR experiments and Dr. F. Fraternali (London, United Kingdom) for providing the coordinates of MSP1$_{19}$ in complex with inhibitory antibodies (12.8 and 12.10). Aliquots of azurin were kindly supplied by Prof. M. Ubbink (Leiden, The Netherlands).

REFERENCES

1. Hobbs, C., and Duffy, P. (2011) Drugs for malaria: something old, something new, something borrowed. *F1000 Biol. Rep.* **3,** 24
2. Wells, T. N., Alonso, P. L., and Gutteridge, W. E. (2009) New medicines to improve control and contribute to the eradication of malaria. *Nat. Rev. Drug Discov.* **8,** 879–891
3. Opar, A. (2011) Quarter-century quest for malaria vaccine shows signs of success. *Nat. Rev. Drug Discov.* **10,** 887–888
4. Holder, A. A. (2009) Malaria vaccines: where next? *PLoS Pathog.* **5,** e1000638
5. Holder, A. A. (2009) The carboxy-terminus of merozoite surface protein 1: structure, specific antibodies and immunity to malaria. *Parasitology* **136,** 1445–1456
6. Holder, A. A., and Blackman, M. J. (1994) What is the function of MSP-1 on the malaria merozoite? *Parasitol. Today* **10,** 182–184
7. Blackman, M. J., Heidrich, H. G., Donachie, S., McBride, J. S., and Holder, A. A. (1990) A single fragment of a malaria merozoite surface protein remains on the parasite during red cell invasion and is the target of invasion-inhibiting antibodies. *J. Exp. Med.* **172,** 379–382
8. Blackman, M. J., Ling, I. T., Nicholls, S. C., and Holder, A. A. (1991) Proteolytic processing of the *Plasmodium falciparum* merozoite surface protein-1 produces a membrane-bound fragment containing two epidermal growth factor-like domains. *Mol. Biochem. Parasitol.* **49,** 29–33
9. Blackman, M. J., Whittle, H., and Holder, A. A. (1991) Processing of the *Plasmodium falciparum* major merozoite surface protein-1: identification of a 33-kilodalton secondary processing product which is shed prior to erythrocyte invasion. *Mol. Biochem. Parasitol.* **49,** 35–44
10. Dluzewski, A. R., Ling, I. T., Hopkins, J. M., Grainger, M., Margos, G., Mitchell, G. H., Holder, A. A., and Bannister, L. H. (2008) Formation of the food vacuole in *Plasmodium falciparum*: a potential role for the 19 kDa fragment of merozoite surface protein 1 (MSP1$_{19}$). *PLoS ONE* **3,** e3085
11. Moss, D. K., Remarque, E. J., Faber, B. W., Cavanagh, D. R., Arnot, D. E., Thomas, A. W., and Holder, A. A. (2012) *Plasmodium falciparum* merozoite surface protein (MSP) 1$_{19}$-specific antibodies that interfere with parasite growth *in vitro* can inhibit MSP1 processing, merozoite invasion and intracellular parasite development. *Infect. Immun.* **80,** 1280–1287
12. Morgan, W. D., Birdshall, B., Frenkiel, T. A., Gradwell, M. G., Burghaus, P. A., Syed, S. E., Uthaipibull, C., Holder, A. A., and Feeney, J. (1999) Solution structure of an EGF module pair from the *Plasmodium falciparum* merozoite surface protein-1. *J. Mol. Biol.* **289,** 113–122
13. Garman, S. C., Simcoke, W. N., Stowers, A. W., and Garboczi, D. N. (2003) Structure of the C-terminal domains of merozoite surface protein-1 from *Plasmodium knowlesi* reveals a novel histidine binding site. *J. Biol. Chem.* **278,** 7264–7269
14. Babon, J. J., Morgan, W. D., Kelly, G., Eccleston, J. F., Feeney, J., and Holder, A. A. (2007) Structural studies on *Plasmodium vivax* merozoite surface protein-1. *Mol. Biochem. Parasitol.* **153,** 31–40
15. Pizarro, J. C., Chitarra, V., Verger, D., Holm, I., Pêtres, S., Dartevelle, S., Nato, F., Longacre, S., and Bentley, G. A. (2003) Crystal structure of a Fab complex formed with PfMSP1-19, the C-terminal fragment of merozoite surface protein 1 from *Plasmodium falciparum*: a malaria vaccine candidate. *J. Mol. Biol.* **328,** 1091–1103
16. Chitarra, V., Holm, I., Bentley, G. A., Pêtres, S., and Longacre, S. (1999) The crystal structure of C-terminal merozoite surface protein 1 at 1.8 Å resolution, a highly protective malaria vaccine candidate. *Mol. Cell* **3,** 457–464
17. O'Donnell, R. A., Saul, A., Cowman, A. F., and Crabb, B. S. (2000) Functional conservation of the malaria vaccine antigen MSP-119 across distantly related *Plasmodium* species. *Nat. Med.* **6,** 91–95
18. Larkin, M. A., Blackshields, G., Brown, N. P., Chenna, R., McGettigan, P. A., McWilliam, H., Valentin, F., Wallace, I. M., Wilm, A., Lopez, R., Thompson, J. D., Gibson, T. J., and Higgins, D. G. (2007) ClustalW and ClustalX version 2.0. *Bioinformatics* **23,** 2947–2948
19. Hensmann, M., Li, C., Moss, C., Lindo, V., Greer, F., Watts, C., Ogun, S. A., Holder, A. A., and Langhorne, J. (2004) Disulphide bonds in merozoite surface protein 1 of the malaria parasite impede efficient antigen processing and affect the *in vivo* antibody response. *Eur. J. Immunol.* **34,** 639–648

20. Morgan, W. D., Lock, M. J., Frenkiel, T. A., Grainger, M., and Holder, A. A. (2004) Malaria parasite-inhibitory antibody epitopes on *Plasmodium falciparum* merozoite surface protein-1$_{19}$ mapped by TROSY NMR. *Mol. Biochem. Parasitol.* **138,** 29–36
21. Morgan, W. D., Frenkiel, T. A., Lock, M. J., Grainger, M., and Holder, A. A. (2005) Precise epitope mapping of malaria parasite inhibitory antibodies by TROSY NMR cross-saturation. *Biochemistry* **44,** 518–523
22. Ling, I. T., Ogun, S. A., and Holder, A. A. (1994) Immunization against malaria with a recombinant protein. *Parasite Immunol.* **16,** 63–67
23. Spencer Valero, L. M., Ogun, S. A., Fleck, S. L., Ling, I. T., Scott-Finnigan, T. J., Blackman, M. J., and Holder, A. A. (1998) Passive immunization with antibodies against three distinct epitopes on *Plasmodium yoelii* merozoite surface protein 1 suppresses parasitemia. *Infect. Immun.* **66,** 3925–3930
24. Benjamin, P. A., Ling, I. T., Clottey, G., Valero, L. M., Ogun, S. A., Fleck, S. L., Walliker, D., Morgan, W. D., Birdsall, B., Feeney, J., and Holder, A. A. (1999) Antigenic and sequence diversity at the C-terminus of the merozoite surface protein-1 from rodent malaria isolates, and the binding of protective monoclonal antibodies. *Mol. Biochem. Parasitol.* **104,** 147–156
25. Lazarou, M., Guevara Patiño, J. A., Jennings, R. M., McIntosh, R. S., Shi, J., Howell, S., Cullen, E., Jones, T., Adame-Gallegos, J. R., Chappel, J. A., McBride, J. S., Blackman, M. J., Holder A. A., and Pleass, R. J. (2009) Inhibition of erythrocyte invasion and *Plasmodium falciparum* merozoite surface protein 1 processing by human immunoglobulin G1 (IgG1) and IgG3 antibodies. *Infect. Immun.* **77,** 5659–5667
26. Chaudhari, A., Fialho, A. M., Ratner, D., Gupta, P., Hong, C. S., Kahali, S., Yamada, T., Haldar, K., Murphy, S., Cho, W., Chauhan, V. S., Das Gupta, T. K., and Chakrabarty, A. M. (2006) Azurin, *Plasmodium falciparum* malaria and HIV/AIDS: inhibition of parasitic and viral growth by azurin. *Cell Cycle* **5,** 1642–1648,
27. Chakrabarty, A. M., Gupta, T. K. D., Yamada, T., Chaudhari, A., Fialho, A. M., and Hong, C. S. (November 30, 2006) Composition and methods for treating malaria with cupredoxin and cytochrome. U. S. Patent WO 2006/127477 A3
28. Hasegawa, H., and Holm, L. (2009) Advances and pitfalls of protein structural alignment. *Curr. Opin. Struct. Biol.* **19,** 341–348
29. Morgan, W. D., Kragt, A., and Feeney, J. (2000) Expression of deuterium-isotope-labelled protein in the yeast *Pichia pastoris* for NMR studies. *J. Biomol. NMR* **17,** 337–347
30. Jiménez, B., Piccioli, M., Moratal, J. M., and Donaire, A. (2003) Backbone dynamics of rusticyanin: the high hydrophobicity and rigidity of this blue copper protein is responsible for its thermodynamic properties. *Biochemistry* **42,** 10396–10405
31. Hall, J. F., Hasnain, S. S., and Ingledew, W. J. (1996) The structural gene for rusticyanin from *Thiobacillus ferrooxidans*: cloning and sequencing of the rusticyanin gene. *FEMS Microbiol. Lett.* **137,** 85–89
32. Díaz-Moreno, I., Díaz-Quintana, A., De la Rosa, M. A., and Ubbink, M. (2005) Structure of the complex between plastocyanin and cytochrome *f* from the cyanobacterium *Nostoc* sp. PCC 7119 as determined by paramagnetic NMR. *J. Biol. Chem.* **280,** 18908–18915
33. Crowley, P. B., Otting, G., Schlarb-Ridley, B. G., Canters, G. W., and Ubbink, M. (2001) Hydrophobic interactions in a cyanobacterial plastocyanin-cytochrome *f* complex. *J. Am. Chem. Soc.* **123,** 10444–10453
34. Lange, C., Cornvik, T., Díaz-Moreno, I., and Ubbink, M. (2005) The transient complex of poplar plastocyanin with cytochrome *f*: effects of ionic strength and pH. *Biochim. Biophys. Acta* **1707,** 179–188
35. van de Kamp, M., Hali, F. C., Rosato, N., Agro, A. F., and Canters, G. W. (1990) Purification and characterization of a nonreconstitutable azurin, obtained by heterologous expression of the *Pseudomonas aeruginosa azu* gene in *Escherichia coli*. *Biochim. Biophys. Acta* **1019,** 283–292
36. Goddard, T. D., and Kneller, D. G. (2006) SPARKY 3. University of California, San Francisco
37. Palma, P. N., Krippahl, L., Wampler, J. E., and Moura, J. J. (2000) BiGGER: A new (soft) docking algorithm for predicting protein interactions. *Proteins* **39,** 372–384
38. Crane, B. R., Di Bilio, A. J., Winkler, J. R., and Gray, H. B. (2001) Electron tunneling in single crystals of *Pseudomonas aeruginosa* azurins. *J. Am. Chem. Soc.* **123,** 11623–11631
39. Badsberg, U., Jørgensen, A. M., Gesmar, H., Led, J. J., Hammerstad, J. M., Jespersen, L. L., and Ulstrup, J. (1996) Solution structure of reduced plastocyanin from the blue-green alga *Anabaena variabilis*. *Biochemistry* **35,** 7021–7031
40. Zhao, D., and Shoham, M. (1998) Rusticyanin: extremes in acid stability and redox potential explained by the crystal structure. *Biophys. J.* **74,** 233
41. Pettersen, E. F., Goddard, T. D., Huang, C. C., Couch, G. S., Greenblatt, D. M., Meng, E. C., and Ferrin, T. E. (2004) UCSF Chimera: a visualization system for exploratory research and analysis. *J. Comput. Chem.* **25,** 1605–1612
42. Alcaraz, L. A., and Donaire, A. (2005) Rapid binding of copper(I) to folded aporusticyanin. *FEBS Lett.* **579,** 5223–5226
43. Zaballa, M. E., Abriata, L. A., Donaire, A., and Vila, A. J. (2012) Flexibility of the metal-binding region in apo-cupredoxins. *Proc. Natl. Acad. Sci. U.S.A.* **109,** 9254–9259
44. Cruz-Gallardo, I., Díaz-Moreno, I., Díaz-Quintana, A., and De la Rosa, M. A. (2012) The cytochrome *f*-plastocyanin complex as a model to study transient interactions between redox proteins. *FEBS Lett.* **586,** 646–652
45. Díaz-Moreno, I., Díaz-Quintana, A., Molina-Heredia, F. P., Nieto, P. M., Hansson, O., De la Rosa, M. A., and Karlsson, B. G. (2005) NMR analysis of the transient complex between membrane photosystem I and soluble cytochrome c_6. *J. Biol. Chem.* **280,** 7925–7931
46. Yamada, T., Goto, M., Punj, V., Zaborina, O., Kimbara, K., Das Gupta, T. K., and Chakrabarty, A. M. (2002) The bacterial redox protein azurin induces apoptosis in J774 macrophages through complex formation and stabilization of the tumor suppressor protein p53. *Infect. Immun.* **70,** 7054–7062
47. Yamada, T., Hiraoka, Y., Das Gupta, T. K., and Chakrabarty, A. M. (2004) Rusticyanin, a bacterial electron transfer protein, causes G_1 arrest in J774 and apoptosis in human cancer cells. *Cell Cycle* **3,** 1182–1187
48. Autore, F., Melchiorre, S., Kleinjung, J., Morgan, W. D., and Fraternali, F. (2007) Interaction of malaria parasite-inhibitory antibodies with the merozoite surface protein MSP1$_{19}$ by computational docking. *Proteins* **66,** 513–527
49. Fleck, S. L., Birdsall, B., Babon, J., Dluzewski, A. R., Martin, S. R., Morgan, W. D., Angov, E., Kettleborough, C. A., Feeney, J., Blackman, M. J., and Holder, A. A. (2003) Suramin and suramin analogues inhibit merozoite surface protein-1 secondary processing and erythrocyte invasion by the malaria parasite *Plasmodium falciparum*. *J. Biol. Chem.* **278,** 47670–47677
50. Blake, R. C., 2nd, and Shute E. A. (1987) Respiratory enzymes of *Thiobacillus ferrooxidans*: a kinetic study of electron transfer between iron and rusticyanin in sulfate media. *J. Biol. Chem.* **262,** 14983–14989

Antimalarial Activity of Cupredoxins: THE INTERACTION OF PLASMODIUM MEROZOITE SURFACE PROTEIN 119 (MSP119) AND RUSTICYANIN

Isabel Cruz-Gallardo, Irene Díaz-Moreno, Antonio Díaz-Quintana, Antonio Donaire, Adrián Velázquez-Campoy, Rachel D. Curd, Kaveri Rangachari, Berry Birdsall, Andres Ramos, Anthony A. Holder and Miguel A. De la Rosa

J. Biol. Chem. 2013, 288:20896-20907.
doi: 10.1074/jbc.M113.460162 originally published online June 7, 2013
